


A New Monte-Carlo Radiative Transfer Simulation of Cyclotron Resonant Scattering Features.

Sandeep Kumar,^{1,2} Suman Bala^{2,3}  and Dipankar Bhattacharya^{2,4}

¹ Digambar Jain College, Dept. of Physics, Baraut, Baghat, Uttar Pradesh 250611, India

² Inter University Center for Astronomy and Astrophysics, Ganeshkhind, Post Bag 4, Pune 411007, India.

³ Indian Institute of Technology Bombay, Dept. of physics, Powai, Mumbai, Maharashtra 400076, India

⁴ Ashoka University, Dept. Of Physics, Sonapat, Haryana-131029, India

Accepted 2022 July 1. Received 2022 June 10; in original form 2022 March 14

ABSTRACT

We present a new Monte-Carlo radiative transfer code, which we have used to model the cyclotron line features in the environment of a variable magnetic field and plasma density. The code accepts an input continuum and performs only the line transfer by including the three cyclotron resonant processes (cyclotron absorption, cyclotron emission, cyclotron scattering). Subsequently, the effects of gravitational red-shift and light bending on the emergent spectra are computed. We have applied our code to predict the observable spectra from three different emission geometries; 1) an optically thin slab near the stellar surface, 2) an accretion mound formed by the accumulation of the accreted matter, 3) an accretion column representing the zone of a settling flow onto the star. Our results show that the locally emergent spectra from the emission volume are significantly anisotropic. However, in the presence of strong light bending the anisotropy reduces considerably. This averaging also drastically reduces the strength of harmonics higher than second in the observable cyclotron spectra. We find that uniform field slabs produce line features that are too narrow, and mounds with large magnetic distortions produce features that are too wide compared to the average widths of the spectral features observed from various sources. The column with a gently varying (dipole) field produces widths in the intermediate range, similar to those observed.

Key words: relativistic processes , X-rays: binaries, stars: neutron, pulsars: general, methods: numerical

1 INTRODUCTION

Cyclotron Resonance Scattering Features (CRSFs) are quasi-harmonic absorption and emission features found in the hard X-ray (10-100 KeV) spectra of highly magnetized ($B \sim 10^{12}G$) accreting neutron stars. The CRSF was first observed in the X-ray spectra of Her-X1 (Truemper et al. 1977). Till now, nearly 36 X-ray pulsars are known to exhibit cyclotron lines in their X-ray spectrum (see Staubert et al. 2019) for a detailed review) The observed cyclotron lines can be used to provide a direct estimate of the field strength in the emission region, usually located close to the neutron star surface, and help to probe the local magnetic field structure and accretion physics. The observed cyclotron lines are found in general to be broad, and the fundamental usually has a shape more complex than a single Gaussian. The higher harmonics have simpler profiles which can be usually well approximated by a Gaussian. The line energy of the fundamental CRSF (ω_1^{res}) is approximately given by

the “12-B-12 rule”

$$\omega_1^{res} \approx 11.57 \text{ KeV } B_{12} \quad (1)$$

where B_{12} represents the magnetic field in units of 10^{12} Gauss. The cyclotron line energies of the n 'th harmonics (ω_n^{res}) are slightly anharmonic due to relativistic corrections and are given by,

$$\omega_n^{res}(\mu'_i) = \frac{m(\sqrt{(1 + 2n(B/B_c) \sin^2 \theta'_i) - 1})}{\sin^2 \theta'_i} \quad (2)$$

(In this work, all quantities are given in natural units, i.e. $\hbar = c = 1$.) Here, θ'_i is the angle between the photon propagation direction and the magnetic field (B), and $\mu'_i = \cos \theta'_i$. The mass of the electron is denoted by m , and $B_c (= m^2/e = 44.1 \times 10^{12}G)$ is the critical magnetic field. The resonance energy $\omega_n^{res}(\mu'_i)$ depends both on the field strength B and μ'_i . The angle dependence of the resonance energy as well as the optical depth introduces a strong anisotropy in photon propagation and the emitted spectra.

There is an extensive body of existing work on the formation of cyclotron lines in X-ray binaries. Two approaches have normally

* E-mail: sumanbala2210@iitb.ac.in

been followed to model the cyclotron lines: 1) solving the integro differential equations of radiative transfer, 2) Monte Carlo simulations. The approach of modeling of cyclotron lines by solving the radiative transfer equations has been adopted in works such as Bonazzola et al. (1979); Meszaros et al. (1980); Nagel (1980, 1981b,a); Meszaros & Nagel (1985); Alexander et al. (1989); Alexander & Meszaros (1991); Bulik et al. (1992, 1995) and Nishimura (2003, 2005, 2008, 2011). Monte-Carlo simulation is the other approach used in the modelling of the cyclotron lines. The existing work in this category include those by Yahel (1979); Pravdo & Bussard (1981); Araya & Harding (1996); Isenberg et al. (1998b,a); Freeman et al. (1999); Araya & Harding (1999); Schönherr et al. (2007) and Schwarm et al. (2017a,b). Among these the most relevant for our work are the ones by Araya & Harding (1999); Schönherr et al. (2007); Schwarm et al. (2017a,b), and Nishimura (2003, 2005, 2008, 2011).

Araya & Harding (1999) [hereafter AH99], for the first time, included fully relativistic cross-sections and transition rates in their Monte-Carlo simulations. They have produced a new set of results for near critical magnetic fields using the relativistic cross-sections derived by Sina (1996). Their simulations were performed for uniform field and uniform density. The effect of optical depth and geometry on the cyclotron line features were studied in this work. Their model produced narrow line features.

Schönherr et al. (2007) [hereafter Schon07] used the code of AH99, and developed a fittable model for the well known X-ray spectral analysis package, XSPEC. They studied the effects of different geometry, optical depth, plasma temperature, linear gradient in the magnetic field and photon angular re-distribution. They also developed a Green's function technique using which the spectra for different injected continuum shapes could be obtained from the results of a single simulation with a flat continuum input.

Nishimura (2003, 2005, 2008, 2011) has investigated a number of issues regarding the cyclotron line formation. Nishimura (2003) studied the effect of dipolar magnetic field on the cyclotron features. Nishimura (2005) studied the effect of a vertical field gradient, including both dipolar and a crust-anchored multipolar (Gil et al. 2002) component. Nishimura (2008) studied the mechanism of formation of broad and shallow lines as observed in most cyclotron line sources. He used the geometry of a stack of multiple sections, each with its own value of magnetic field, density and temperature. Finally composite spectra were presented for both slab and cylindrical geometry, showing the complexities resulting from multi-zoning.

The most recent work in Cyclotron Line MC simulation has been done by Schwarm et al. (2017a,b) [hereafter SC17] in a series of two papers. They have computed and stored interpolation tables needed for their MC simulation code using the fully relativistic photon-electron partial scattering cross section from Sina (1996). These interpolation tables have been used by their MC code to save computation time. They have done the cyclotron line simulation for a cylindrical geometry, including parameter gradients for density, magnetic field, parallel electron temperature and matter velocity. They have also incorporated different types of photon sources, namely i) point source ii) line source iii) plane source relative to magnetic field direction at the base of column. In their simulation the continuum of any shape can be generated using the Green's function approach. They have also fitted the NuSTAR spectra of Cep X-4 with their new XSPEC model `cyclofs` assuming a slab geometry and a FD-cut continuum. They found that the estimated magnetic field differs significantly from the estimated value form a simple Gaussian absorption line.

Mukherjee & Bhattacharya (2012) [hereafter MB12] have estimated the field distortion in the polar cap accretion mound, and

studied its effect on the fundamental cyclotron feature. They first solved the Grad-Sharanov equation for an axisymmetric magnetostatic equilibrium to estimate the magnetic field distortion for different mound heights corresponding to different mass loading on the field lines. The distorted field structure in the mound were then used to phenomenologically compute the expected shape of the fundamental feature. Light bending effects were included but no radiative transfer was performed. The spin phase dependence of the line feature was investigated. It was found that with the increase of mound height and hence of field distortion, the fundamental feature tends to broaden and develop a double-peaked structure. Strong angle averaging due to light bending tends to wash out the angle dependence of the spectrum seen by a distant observer. Little or no spin phase dependence is left in the spectrum unless there happens to be dissimilar contributions from the two opposite poles.

Any model that attempts to explain the observed features of cyclotron lines such as large widths, variation of line energy and line width with luminosity, anharmonic line ratios etc, must incorporate realistic fields, plasma density and emission geometries. In earlier theoretical models one of two extreme emission geometries are considered: a fan beam or a pencil beam, but there are sources with intermediate geometries where significant contributions may come from both fan beam and pencil beams (Becker et al. 2012). No attempt till date has been made to incorporate both the geometries in a model. We have developed a Monte-Carlo code CLSIM in which arbitrary magnetic field and plasma density variation can be incorporated. The fan beam and pencil beam geometries can also be simultaneously incorporated. Many of the basic techniques in our code are based on the Monte-Carlo implementation of AH99 but we differ from AH99 in those parts of the implementation where non-uniform magnetic field and plasma density are incorporated. Additionally, light bending effects are also incorporated in our scheme. Finally we have implemented a scheme of weighting entire photon trajectory trees as a function of the initial injected photon energy, allowing us to compute the resulting spectra from an input continuum of any shape, using a single initial simulation with a flat continuum.

2 PHYSICAL ASSUMPTIONS OF OUR MODEL

In this work, we solve the radiative line transfer problem with inputs such as geometry, magnetic field structure, plasma density, temperature and velocity profiles from previous works (Becker & Wolff (2007), MB12, AH99). In very strong magnetic fields ($\approx 10^{12}G$) the problem of line transfer is challenging (Wang et al. 1988), so, we have made some simplifications and approximations. The physical assumptions and approximations made in our work are as follows;

- **Static Column:** We assume that the plasma inside the accretion column is in a magnetostatic configuration. This may apply to a slowly sinking plasma in the accretion column.
- **Resonance processes:** We are mainly interested in the modelling of CRSF features so only the line transfer is considered. Modification of the injected continuum is considered solely due to the three resonant processes (cyclotron absorption, scattering and cyclotron emission). The production and absorption of continuum photons during the radiation diffusion inside the simulation volume have been ignored.
- **Plasma thermodynamic state:** We consider a low density plasma ($n_e \sim 10^{22} \text{ cm}^{-3}$), and electrons are assumed to be in the ground state of Landau levels $n = 0$ since for high magnetic fields ($\sim 10^{12} \text{ G}$) the cyclotron decay rates dominate over collisional excitation rates (AH99, Schönherr et al. (2007)). We assume that

the plasma is in statistical equilibrium and is defined by a parallel electron temperature T_e and a relativistic energy distribution;

$$f_e(p)dp = N \exp\left(-m \frac{\sqrt{1+p^2} - 1}{T_e}\right) dp \quad (3)$$

Here p is the momentum parallel to the magnetic field and T_e is the temperature characterizing the motion of the electrons parallel to the magnetic field. Although the temperature may vary in the accretion column (Isenberg et al. (1998b,a); Nishimura (2011), AH99) in this work we have assumed it to be constant. We have conducted our simulations for different values of T_e . As the electrons are assumed to be in the Landau ground state with zero perpendicular momentum, the distribution given in Eq-3 is one dimensional.

- **Optical depth:** Previous Monte-Carlo simulations for modelling the cyclotron line are restricted to the optical depth in the range ($10^{-4} - 10^{-3}$), as the computation time is always an issue with Monte-Carlo simulations when it deals with every single microscopic event. In this work, we have used the relativistic magneto-Compton cross-section by Sina (1996) which is also very computation intensive. So, considering available computational resources, we have restricted our simulations to regions of maximum Thompson optical depth of $\sim 10^{-3}$, which corresponds to a line centre optical depth of $> 10^2$ at the fundamental. Although higher optical depth can produce a more accurate shape of the CRSFs, it is not achievable as computation time increases quadratically with τ (as the number of scatterings increases as $\tau^2 + \tau$).

- **Magnetic field:** In our simulations, we have explored the magnetic field in the range ($0.84 \times 10^{12} - 6.6 \times 10^{12}$)G, which covers most of the observed range of cyclotron lines.

- **Photon polarization modes and electron spin state:** The magnetized vacuum photon polarization modes, appropriate for the high field, low-density plasma are used in computing the scattering cross-section. In this regime, it is adequate to consider polarization averaged radiative diffusion, which we adopt in the computations present in this work. We adopt the best possible choice of spin states and polarization states from Sokolov & Ternov (1968) and Shabad (1975) respectively.

- **Cross-sections and decay rates:** The relativistic cross-sections (Sina 1996; Harding & Daugherty 1991) and transition rates (Harding & Preece 1987) are considered in this work.

3 A NEW MONTE CARLO CODE CLSIM

Based on the assumptions stated above, we have developed a complete Monte-Carlo radiative transfer code to model resonant cyclotron processes including absorption, emission and magneto-Compton scattering. While we use some of the techniques outlined in AH99, the implementation is entirely our own. One of the recent works on the Monte-Carlo simulation of cyclotron line is SC17. A comparison of this work with AH99 and SC17 is given below.

We have computed the line profiles including up to ten harmonics, while AH99 included up to four, and SC17 have included up to five harmonics. In SC17 and this work the angle of scattering has been selected using the differential scattering cross-section by Sina (1996) while AH99 have used the differential transition rates by Latal (1986). We have also included additional features that enhance the applicability of our code. We perform our computation in real space instead of optical depth space as done by AH99 & SC17. SC17 and our work include the effects of gravitational red-shift, but only our code includes the effect of light bending, allowing us to

Table 1. Application cases of our code.

Type	Geometry	Magnetic field structure	Density variation	T_e
column Case-I	Slab10	Uniform	Uniform	Uniform
mound Case-II	Slab10	MB12	Paczynski (1983)	Uniform
Accretion Column Case-III	Cylinder with supercritical luminosity	Dipolar	Becker & Wolff (2007)	Uniform

generate results that can be directly compared with observations. In this work, we implement a scheme of weighting entire photon trajectory trees as a function of the initial injected photon energy, allowing us to compute the resulting spectra from an input continuum of any shape, from a single initial simulation with a flat continuum, whereas SC17 has used the Green's function approach for the same. In SC17 the simulation volume has been split into different cylinders with arbitrary dimensions, whereas we have split the simulation volume into small cells. AH99 and SC17 have considered a constant magnetic field and plasma density within the simulation volume, but our code is capable of including any arbitrary spatial variation of the magnetic field and plasma parameters within the simulation volume. In this work we have solved the radiative diffusion problem for three applications cases, as mentioned in Table 1.

3.1 Application cases

We use our Monte Carlo code to compute the emergent spectra in three broadly defined cases (Table-1) mentioned below;

- **CASE-I:** An isothermal static plane circular slab 1-0 (illuminated from below) having a uniform magnetic field and uniform density. In the case of low luminosity sources the inflow of plasma is stopped near the stellar surface generally via Coulomb collisions. In these situations slabs with scale height of $z_c \sim 200$ cm are expected (Meszaros et al. 1983; Harding et al. 1984). So, we have taken a similar emission geometry with a plane circular slab 1-0 (illuminated from below) of height $z_c = 100$ cm and radius $r_c = 1$ Km. The simulation is performed for uniform field, uniform plasma density and uniform temperature in the simulation region.

- **CASE-II:** An optically thin top layer of the accretion mound approximated as an isothermal static plane circular slab 1-0, with a distorted magnetic field, taken from MB12 and a density profile obtained using the equation of state given by (Paczynski 1983). The accreted matter at the base of the accretion column is assumed to form a magnetically confined plasma mound. The heavy mass loading at the base of the mound can severely distort the dipolar magnetic field structure (Payne & Melatos (2004); MB12). Cyclotron lines which originate in optically thin layer of accretion mound bears the signature of distorted magnetic fields and can be used to measure the extent of magnetic field distortion. We follow the approach of MB12 to solve for the structure of the static axisymmetric polar mound from the 2D Grad Shafranov equation using our choice of equation of state. The solution is obtained in terms of the magnetic flux function $\psi(r, z)$ in cylindri-

cal coordinates, from which the magnetic field may be computed as :

$$B_r = -\frac{1}{r} \frac{\partial \psi(r, z)}{\partial z}, \quad B_z = \frac{1}{r} \frac{\partial \psi(r, z)}{\partial r}$$

We construct mound structures for different heights (e.g. 45m, 55m, etc).

In this case we simulate the cyclotron line formation in the optically thin top layer of the plasma mound, which is approximated as a 1-0 plane circular slab geometry, with the distribution of magnetic field and density as obtained from the GS solution. The Cartesian components of the magnetic field are obtained for any point (r, ϕ, z) in the mound as

$$\begin{aligned} B_x &= B_r \cos(\phi) \\ B_y &= B_r \sin(\phi) \\ B_z &= B_z \end{aligned}$$

We model this thin layer as a slab of uniform thickness, with continuum Thomson optical depth $\tau_T = 10^{-3}$. The density as a function of depth l in this slab works out to be

$$\begin{aligned} n_e(l) &= (X_F(l)/A_F)^3 / m_{He} \\ X_F(l) &= \frac{15}{16\sqrt{2}} \sqrt{\left(\xi^2(l) - \frac{8}{3} + \xi(l) \sqrt{\left(\frac{16}{9} + \xi^2(l) \right)} \right)} \\ \xi(l) &= 80.89959983(l/L_0) + 1 \end{aligned} \quad (4)$$

from the Grad Shafranov solution. where $L_0 = 1\text{Km}$ is a scaling parameter, and plasma is assumed to be a electron-Helium mixture.

- **Case-III:** In this case, we deal with the situation at the opposite extreme, where the accretion rate is high and the accretion column is optically thick. In high luminosity sources, the flow of material near the neutron star is decelerated by radiative shocks a few kilometers away from the surface and an elongated column is formed in which the matter subsonically settles and generates radiation. For this case, we place the source plane at a fixed optical depth inside the boundaries of the cylindrical column. The density (Eq-5) and hence the optical depth across the column increases towards lower altitudes. The width of the optically thin layer ($\tau_T = 10^{-3}$) is found to be very small (millimeters) near the base of the column but much larger at higher altitudes due to decreasing density. The injection surface then can be approximated as a truncated cone buried inside the cylindrical column (Fig-1). The injected photons diffuse in the region bounded by the injection surface and the outer surface of the cylindrical column. This type of geometry can be considered as a cylindrical shell, in which the radiation escapes sideways and also from a slab which is situated at the top. The height and the radius of the accretion column are assumed to be $h_c = 1\text{ km}$ and $r_c = 1\text{ km}$ respectively. The magnetic field in the column is assumed to be dipolar, with a strength $B' = 0.03$ (all the magnetic field values in this work are given in the unit of B_c). at the base. For distribution of plasma density in the column we adopt the profile derived by [Becker & Wolff \(2007\)](#) for the case of super-Eddington luminosity,

$$n_e(z) = \left(\frac{\dot{M}_c}{\pi r_c^2 v_{ff} (1 - (7/3))^{-z/z_c}} \right) / m_{He} \quad (5)$$

$$v_{ff} = \sqrt{\frac{2GM_*}{R_*}} \quad (6)$$

where $\dot{M}_c, v_{ff}, z_c, r_c$ are the accretion rate, free fall velocity, height of the accretion column and radius of the accretion column respectively. M_*, R_* are the mass and the radius of the neutron star.

In all cases, we explore the line forming region with a maximum Thomson optical depth of $\tau_T \sim 10^{-3}$.

3.2 Our radiative transfer scheme

In our Monte-Carlo radiative transfer scheme we perform the polarization averaged radiative transfer in the following steps.

(i) A photon is injected at a location $(x_{inj}, y_{inj}, z_{inj})$ at the source plane with energy ω_{inj} in the direction $(\theta_{inj}, \phi_{inj})$ (Sec.3.3).

(ii) After injection, the propagation length of the photon before any scattering or absorption is determined by a chosen free path $\lambda(B', \omega_i, \mu_i)$. The photon either escapes, or is absorbed or scattered after propagating the distance λ . The probability of scattering and absorption are computed and one from absorption or scattering is selected.

(iii) For scattering or absorption the parallel momentum p_i of the electron is selected.

(iv) The electron is excited to a higher state n_f either through scattering or through absorption. If absorption occurs then the photon trajectory is terminated, if scattering occurs then the angle of scattering θ_f is selected.

(v) The electron de-excites via radiative transitions to a lower Landau level n'_f and generates a transition photon of energy ω_t and emitted in direction (θ_t, ϕ_t) . The electron continues to de-excite and emit transition photons until it reaches the ground state. All these transition photons are again injected into the Monte-Carlo scheme. This process of photon propagation continues until photons escape from the boundary of the simulation region.

(vi) Finally the light bending effects are incorporated.

It is to be noted that our Monte-Carlo scheme is based on AH99 but with some differences which are necessary for the implementation of varying magnetic field and varying density. In the rest of this section we only mention those issues which are either important to highlight or differs from AH99 scheme and related to our implementation only. For full implementation of Monte-Carlo scheme using relativistic cross-sections for uniform magnetic field and uniform density, we strongly refer the reader to AH99.

3.3 Photon Injection

The first step in the Monte-Carlo simulation is to inject the photons from a prescribed continuum with an energy ω_{inj} , propagating in some direction $(\theta_{inj}, \phi_{inj})$ from some position $(x_{inj}, y_{inj}, z_{inj})$ on the source plane. The selection procedure of the energy of a photon at injection is explained in the next section and position of photon injection and the direction of its propagation are explained in Sec.3.3.2

3.3.1 Selection of energy for photon injection

The input continuum spectrum may be simulated by either drawing the photon energies from a prescribed spectral distribution, or by

first carrying out the Monte Carlo simulation for an uniform photon energy distribution, and later assigning weights to each emergent photons as a function of its input energy and the prescribed continuum shape. The latter method avoids the need to run the simulation separately for each continuum shape, and is therefore our method of choice. For each escaping photon, the escape location x_e, y_e, z_e , the energy ω_e and the propagation angle θ_e, ϕ_e and its mother photon parameters $(x_{inj}, y_{inj}, z_{inj}, \theta_{inj}, \phi_{inj}, \omega_{inj})$ are stored. The emergent spectrum arising out of a specific injected continuum shape $f_p(\omega)$ may then be obtained by multiplying a weight proportional to $f_p(\zeta w_{inj})$ to each escaping photon, where ζ is the redshift of the mother photon with energy w_{inj} . The output spectrum is then compiled by counting the total weight of the escaping photons in different energy and angle bins:

$$N_{kl}(\omega_k, \mu_l) = A \sum_{\substack{|\omega_e - \omega_k| \leq \Delta\omega_e \\ |\mu_e - \mu_l| \leq \Delta\mu_e}} f_p(\zeta \omega_{inj}) \quad (7)$$

where A is a normalization factor, which we have set to unity as we are interested only in the relative shape rather than the total energy in the spectrum. Apart from the flat continuum, we use the HCUT (High energy cutoff power law) continuum shape in this work.

$$f_p(\omega) \propto \begin{cases} \omega^{-\Gamma-1} & \text{for } \omega \leq \omega_{cut} \\ \omega^{-\Gamma-1} \exp\left(-\frac{\omega - \omega_{cut}}{\omega_{fold}}\right) & \text{for } \omega > \omega_{cut} \end{cases} \quad (8)$$

3.3.2 Selection of angle and position co-ordinates for photon injection

The method of selection of position and angle of photon injection is dictated by the choice of simulation geometry. For Case-I and Case-II we consider a plane circular slab 1-0 geometry. For these two cases photons are uniformly ($r = r_c \sqrt{\xi}, \phi = 2\pi\xi$) and isotropically ($\mu_{inj} = \xi, \phi_{inj} = 2\pi\xi$) injected at the base for propagation in the upward hemisphere, where r, ϕ are the radial and azimuthal angle co-ordinate in cylindrical co-ordinate system, and ξ is a uniform random variate in the range 0 to 1.

For the cylindrical geometry (Case-III), we place the source plane at a fixed optical depth $\tau_T = 10^{-3}$ inside the boundaries of the cylindrical column. The source plane can be approximated as a truncated cone buried inside the cylindrical column (see Fig-1). The scheme for selection of position co-ordinates of injection ($x_{inj}, y_{inj}, z_{inj}$) at the source plane and the direction of injection (θ_{inj}, ϕ_{inj}) for case III, is given in Appendix A. The injected photons diffuse in the region bounded by the injection surface and the outer surface of the cylindrical column.

3.4 Free path of the photon

The effective local mean free path in an inhomogeneous medium is given by

$$\bar{\lambda}(B', \omega_i, \mu_i) = \frac{1}{n_e P_{Tot}(B', \omega_i, \mu_i)} \quad (9)$$

where $P_{Tot}(B', \omega_i, \mu_i)$ is the total line profile. The line profile is computed as follows,

$$P_{Tot} = P_{Abs} + P_{Sc} \quad (10)$$

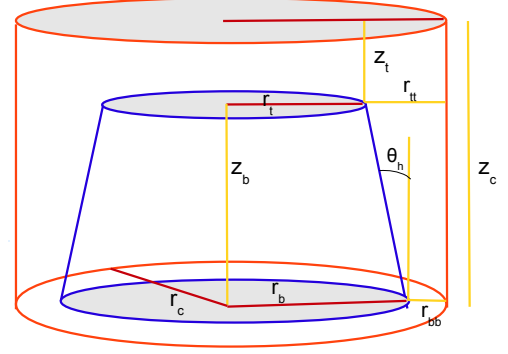


Figure 1. This figure depicts the geometry of the column for the Case-III in Table-1. The structure in the blue color is a cone cut at the top. The surface of the cone is defined such that it lies at a fixed optical depth below the surface of the cylindrical column.

$$P_g(B', \omega_i, \mu_i) = \langle \sigma_g(B', \omega_i, \mu_i) \rangle_{f_e(p)} = \int_{-\infty}^{\infty} \left(\sum_{n=n_v}^{n_{max}} \sigma_g^n(B', \omega_i, \mu_i) \right) f_e(p) dp \quad (11)$$

where n_e is the local electron density, $\sigma_{abs}^n(B', \omega_i, \mu_i)$ ($g = abs$) is the absorption and $\sigma_{sc}^n(B', \omega_i, \mu_i)$ ($g = sc$) is the total scattering cross-section from ground state to state n . Here, $n_v = 0$ for scattering and $n_v = 1$ for absorption. The incident photon ω_i can excite the electron up a maximum Landau level n_{max} determined by $\omega_i \approx n_{max} B'$. We use fully relativistic absorption cross-section (Harding & Daugherty 1991) and scattering cross-section σ_{sc} from Sina (1996). The scattering cross-section is spin and polarization dependent, while we have used a polarization and spin averaged cross-section by summing over the final (f) and averaging over the initial spin and polarization states. The free path λ , namely the distance travelled by a photon before encountering an absorption or scattering, may then be obtained from the probability distribution giving

$$\lambda = -\bar{\lambda} \ln(1 - \xi) = -\bar{\lambda} \ln \xi \quad (12)$$

In the last equality $(1 - \xi)$ has been replaced by ξ as the distribution of both are the same.

3.5 Probability of absorption and scattering

A photon with energy ω_i and moving in the direction μ_i is either absorbed or scattered by an electron after traveling a free path λ . Whether a scattering or an absorption will occur is chosen based on the fractional probabilities

$$R_{abs}(B', \omega_i, \mu_i) = \frac{\sum_{n=1}^{n_{max}} \sigma_{abs}^n(B', \omega_i, \mu_i)}{\sum_{n=1}^{n_{max}} \sigma_{abs}^n(B', \omega_i, \mu_i) + \sum_{n=0}^{n_{max}} \sigma_{sc}^n(B', \omega_i, \mu_i)}$$

$$R_{sc}(B', \omega_i, \mu_i) = \frac{\sum_{n=1}^{n_{max}} \sigma_{sc}^n(B', \omega_i, \mu_i)}{\sum_{n=1}^{n_{max}} \sigma_{abs}^n(B', \omega_i, \mu_i) + \sum_{n=0}^{n_{max}} \sigma_{sc}^n(B', \omega_i, \mu_i)}$$

If the uniform variate $\xi < R_{abs}$ then absorption is selected, otherwise scattering is selected.

3.6 Momentum selection

The selection of parallel momentum of the interacting electron is performed using a partial profile (see AH99 for more details),

$$P_g^p(B', \omega_i, \mu_i, q_i) = \int_{-\infty}^{q_i} \left(\sum_{n=n_v}^{n_{max}} \sigma_g^n(B', \omega_i, \mu_i) \right) f_e(p) dp \quad (13)$$

Here, $g = sc$ is for scattering and $g = abs$ is for the absorption cross-section. The absorption cross-section σ_{abs} and scattering cross-section σ_{sc} have similar values near resonance region and somewhat different values at the continuum. Run time computation of partial profile P_{sc}^p is extremely time consuming as compared to P_{abs}^p because of more complex analytic expression of σ_{sc} containing infinite sums on virtual Landau states (Sina 1996). Since the cross-section at resonance is orders of magnitude greater than the continuum, the contribution of near resonance region dominates over the contribution of continuum in the partial profiles. For the case of uniform field the momentum selection is performed using pre-computed $P_{sc}^p(B', \omega_i, \mu_i, q_i)$ scattering partial profiles and for nonuniform magnetic field it is computed runtime using $P_{abs}^p(B', \omega_i, \mu_i, q_i)$.

After selecting the momentum, Monte-Carlo modeling of the rest of the processes including items 4 and 5 in the Sec. 3.2 are done in a manner similar to that in AH99.

3.7 Numerical implementation

We perform the Monte-Carlo simulations for two classes of magnetic field a) uniform magnetic field and uniform density (Case-I of Table-1), and b) for varying magnetic field and varying density (Case-II, Case-III of Table-1). While the basic steps are the same for both classes, the implementation differs considerably. It is noticeable that nearly all PDFs have dependence on (B', μ_i) . Three reference frames are considered for performing the radiative transfer,

- (i) $Gb (X^G, Y^G, Z^G)$ with origin at the base of the mound and z axis oriented along the magnetic axis
- (ii) $Es (X^E, Y^E, Z^E)$ with origin at the point of scattering or absorption, with its axis X^E, Y^E, Z^E parallel to the axis X^G, Y^G, Z^G of the Gb
- (iii) $Lb (X^L, Y^L, Z^L)$ attached to the point of scattering or absorption with its Z^L axis along the local magnetic field vector and with Y^L, Z^L plane containing the Z^E axis.

In case of varying magnetic field the direction of the magnetic field vector changes from place to place so we have used all the three frames (Gb, Es, Lb) to deal with the situation. For the non-uniform magnetic field case the radiative transfer is performed in three stages.

Stage-I: Injection is performed at a point x_i, y_i, z_i on the source plane in Gb frame in the direction μ_i, ϕ_i .

Stage-II: The μ_i, ϕ_i are converted to Lb frame angles μ_i^L, ϕ_i^L using Eq-14.

$$\Omega^L = T\Omega^G$$

where T is the transformation matrix and is given by

$$T = \begin{pmatrix} \sin \phi_B & -\cos \phi_B & 0 \\ \cos \theta_B \cos \phi_B & \cos \theta_B \sin \phi_B & -\sin \theta_B \\ \sin \theta_B \cos \phi_B & \sin \theta_B \sin \phi_B & \cos \theta_B \end{pmatrix} \quad (14)$$

where θ_B, ϕ_B are the angles of magnetic field vector (z axis of the Lb frame) measured in the Es or the Gb frame. The transformation $Gb \rightarrow Lb$ facilitates the computation since the PDF of several processes do not depend upon μ_i but depend upon the angle between the local magnetic field vector and the photon propagation vector (μ_i^L). The computation of all the following steps related to scattering, absorption and emission are performed in the local frame Lb .

- (i) Selection of the momentum (p_i).
- (ii) Selection of the free path $\lambda(\omega_i, \mu_i^L)$.
- (iii) Selection between absorption or scattering, and for absorption we terminate the trajectory of the photon.
- (iv) Selection of scattering angle (μ_f^L, ϕ_f^L)
- (v) Computation of photon energy ω_f and final electron momentum p_f
- (vi) Selection of the Landau level n_f after excitation
- (vii) Selection of the Landau level n'_f after de-excitation
- (viii) Selection of emission angle μ_t^L, ϕ_t^L of the transition photon.
- (ix) Computation of the energy of the transition photon ω_t and the final momentum p of the electron in state n'_f

Stage-III: The angle (μ_f^L, ϕ_f^L) of the scattered photon and μ_t^L, ϕ_t^L of the transition photons are transformed back to $(\mu_f, \phi_f), (\mu_t, \phi_t)$ in Gb frame using inverse transformation of Eq-14.

In case of uniform magnetic field, since the direction of the field is the same everywhere, only one reference frame $Gb (X^G, Y^G, Z^G)$ is sufficient for the radiative transfer. All the three stages of radiative transfer stated above are performed in Gb frame.

3.7.1 Treating varying magnetic field and plasma parameters

Since the magnetic field varies in the simulation region, the computation of the free path is not very straightforward. For this reason we have divided the simulation volume into cuboid cells within each of which the local density and magnetic field are assumed constant at the value evaluated at the center of the cell. The cell-to-cell radiative transfer is performed by creating a new cell centered at the point where the photon hits a cell edge. This method can in principle be used for arbitrarily large gradients by making cell sizes small enough, but with the practical limitation that for very small cells the computation time increases significantly. We use this method only while treating varying magnetic field and density in the simulation volume (Case-II and Case-III of Table-1).

3.7.2 Numerical computation of partial and total line profile functions

Total line profiles $P(B', \omega_i, \mu_i)$ are used to compute the mean free path $\bar{\lambda}$ and partial profiles $P^P(B', \omega_i, \mu_i, q_i)$ are used in momentum selection. The computation of the partial profiles $P_{sc}^P(B', \omega, \mu_i, q_i)$ and line profiles $P_{sc}(B', \omega_i, \mu_i)$, which involve the computation of scattering cross-section $\sigma_{sc}^n(B', \omega_i, \mu_i)$, is the most computationally expensive part of our code. To include the natural line width $\Gamma^{n,s}(p)$ in the cross-section $\sigma_{sc}^n(B', \omega_i, \mu_i)$, we compute the transition rates $\Gamma^{n,s}$ in $p = 0$ frame and store these values on a grid of (B', n, s) for 50 equally spaced values between (B_{min}, B_{max}) , 20 values of $n \in [1, 2, \dots, 20]$ and two values of the spin (s). Where B_{min}, B_{max} are the minimum and maximum values of the magnetic field in the simulation region. Later the computation of $\Gamma^{n,s}(p)$ which is needed in computation of σ_{sc} can be performed by doing Lorentz transformation on stored values $\Gamma^{n,s}(p = 0)$ with the transformation $\Gamma^{n,s}(p) = [m(1 + 2nB')^{1/2}/E_n(p)]\Gamma^{n,s}(p = 0)$. The line profiles $P(B', \omega_i, \mu_i)$ and partial profiles $P^P(B', \omega_i, \mu_i, q_i)$ are computed and stored once on a grid of (B, μ_i, ω_i) and $(B, \mu_i, \omega_i, q_i)$ respectively and then utilized in the runtime.

To store the line profile $P_{sc}(B', \omega_i, \mu_i)$ on a grid of B', ω_i, μ_i , we follow a scheme similar to that adopted by AH99, however the range of parameters and step sizes are different in our case. We have taken 6 values from $B' = 0.0199$ to $B' = 0.03$ on a equally spaced logarithmic interval and 6 values from $B' = 0.039$ to $B' = 0.15$ on equally space logarithmic interval, 100 equally spaced values for $\mu_i \in (-0.985, 0.985)$. Sampling of ω_i depends upon the value of μ_i , which is based on the fact that the resonant peaks are very sharp, occurring at $\omega_i \rightarrow \omega_n^{cut} (= \sqrt{1 + 2nB'} - 1)/\sin \theta'_i$, for details see Eq 44 of AH99) for $|\mu_i| < 0.5$, but are relatively broad, occurring at $\omega_i \rightarrow \omega_n^{res}$ for $|\mu_i| > 0.5$. The estimate of the width of the resonance peak can be approximated by Doppler width $w_D = B'\sqrt{2mT_e}$. In case of $|\mu_i| < 0.5$ two different grids on ω_i are made: 1) a uniform grid U_{ω_i} on ω_i and 2) a binary spacing grid H_{ω_i} closer to the each peak ω_n^{cut} . In case of a binary spacing grid H_{ω_i} the sampling begins at the point $\omega_n^{cut} - w_D$ on the left and the point $\omega_n^{cut} + w_D$ on the right and approaches until $|1 - \omega_i/\omega_n^{cut}| < 10^{-3}$ in step lengths that are progressively halved. Finally both the grids U_{ω_i} and H_{ω_i} are merged to form a final grid F_{ω_i} . For the case of $|\mu_i| > 0.5$ equal interval sampling is employed throughout and ω_i values are saved on a uniform grid U_{ω_i} .

Storing the partial profiles $P_{sc}^P(B, \omega_i, \mu_i, q_i)$ on a grid needs to save one more parameter p_i along with B, ω_i, μ_i . The sampling scheme for B, ω_i, μ_i is the same for $P_{sc}(B', \omega_i, \mu_i)$. Placing the sampling points for parallel momentum p_i needs extra care since the width, height and position of the resonance peaks in p_i space are highly variable depending upon the values of B, ω_i, μ_i . For each value of n , zero, or one (p_{n0}^s) or two (p_{n+}^s, p_{n-}^s) solutions of the equation $\omega'_i = \omega_n^{res}(\mu'_i)$ are possible (AH99). So all the possible solutions from $n = 1$ to $n = 10$ which lie in the range $(-50T_e, 50T_e)$ are stored. Sampling of p_i is performed on two grids, a uniform grid U_{p_i} in p_i and a binary spacing grid H_{p_i} near each solution in p_i . Finally after merging these two grids and sorting in p_i , a final grid is obtained on which partial profiles $P_{sc}^P(B', \omega_i, \mu_i, q_i)$ are stored.

The mean free path $\bar{\lambda} = 1/(n_e(P_{sc} + P_{abs}))$ is selected by using the line profiles for both scattering and absorption where $P_{abs}(B', \omega_i, \mu_i)$ is computed runtime and $P_{sc}(B', \omega_i, \mu_i)$ is obtained by interpolation of the already stored values of $P_{sc}(B', \omega_i, \mu_i)$. In case of varying magnetic field, for both absorption and scattering, we use $P_{abs}^P(B', \omega_i, \mu_i, q_i)$ for momentum selection since the interpolation of partial profiles $P_{sc}^P(B', \omega_i, \mu_i, q_i)$

across different B' turn out to be not accurate (due to the extreme sensitivity of the position and features of the resonance peaks in momentum space on the parameters B', ω_i, μ_i, p_i). We compute partial profile $P_{abs}^P(B', \omega_i, \mu_i, q_i)$ runtime on exact values of B', ω_i, μ_i to select the momentum. The use of absorption partial profile $P_{abs}^P(B', \omega_i, \mu_i, q_i)$ for momentum selection of scattering process is justified near the resonance energy since both the cross-sections have similar numerical values in that region.

3.7.3 Interpolation in the table of stored values of line profile functions $P_{sc}(B', \omega_i, \mu_i)$

The line profiles are stored on a grid of magnetic field, cosine of angle and energy ($(B'_{st}(i), i = 1 \dots 12), (\mu_{st}(j), j = 1 \dots 100), (\omega_{st}(k), k = 1 \dots k_{max})$) with 12 values of the magnetic field, 100 equally spaced values of μ_i and strategically placed k_{max} energy values as discussed in Sec.3.7.2. An interpolation scheme is needed to compute the line profile $P_{sc}(B', \omega_i, \mu_i)$ at any other value of magnetic field B'_{com} , energy ω_{com} and angle μ_{com} . First we select the two values of magnetic field $B'_{st}(i), B'_{st}(i+1)$ on a grid between which the value B'_{com} lies. Next we locate a μ_{ns} value which is nearest to μ_{com} on the grid μ_{st} . We choose to perform interpolation for this value μ_{ns} . We have now two line profiles $P_{sc}(B'_{st}(i), \mu_{ns}, (\omega_{st}(k), k = 1, k_{max}))$, $P_{sc}(B'_{st}(i+1), \mu_{ns}, (\omega_{st}(k), k = 1, k_{max}))$ and interpolation is to be performed on these line profiles. The line profiles are resonant at energies $(\omega_1^{res}, \omega_2^{res} \dots)$ and the resonance energies ω_n^{res} scale with the strength of the magnetic field. The line profiles, too, scale in energy space in proportion to the resonance energies. We utilize this scaling behavior to interpolate the line profile. We first find the two scaled energy values $\omega_l(\omega_{com}, B'_{com}, B'_{st}(i))$ and $\omega_f(\omega_{com}, B'_{com}, B'_{st}(i+1))$ which provide the energy markers on the two values $P_{sc}(B'_{st}(i), \mu_{ns}, \omega_l)$ and $P_{sc}(B'_{st}(i+1), \mu_{ns}, \omega_f)$ between which the interpolation will be performed to derive $P_{sc}(B'_{com}, \mu_{ns}, \omega_{com})$. The values of ω_l and ω_f are derived as follows. We compute the first 10 resonance energies $\omega_n^{res}(B', \mu_{ns})$ values for three magnetic fields $B'_{st}(i), B'_{com}, B'_{st}(i+1)$, i.e three lists of resonance energies are created for three magnetic fields: $T_f = [\omega_n^{res}(B'_{st}(i+1), \mu_{ns}), n = 1, \dots, 10]$, $T_m = [\omega_n^{res}(B'_{com}, \mu_{ns}), n = 1, \dots, 10]$, $T_l = [\omega_n^{res}(B'_{st}(i), \mu_{ns}), n = 1, \dots, 10]$. Now a second order polynomial fit is performed on the points T_f versus T_m (say with a fitting polynomial $f_f(\omega_i)$) and a similar one on T_l versus T_m with another fitting polynomial $f_l(\omega_i)$. From these, ω_f and ω_l are derived as follows:

$$\begin{aligned} \omega_f &= f_f(\omega_i = \omega_{com}) \\ \omega_l &= f_l(\omega_i = \omega_{com}) \end{aligned}$$

One should note that ω_f and ω_l are computed using the resonance energies $\omega_n^{res}(B')$ which increase with increasing magnetic field, hence $\omega_l < \omega_{com} < \omega_f$. We have stored the P_{sc} values for $\omega_i \in (0.1 - 200)$ KeV so it is possible that at energies at the boundary close to 1 KeV and 200 KeV the values of ω_f, ω_l may go out of bound (i.e. $\omega_l < 0.1$ KeV or $\omega_f > 200$ KeV) hence we restrict our simulation to $(1 - 150)$ KeV and at times we simulate only in the continuum range $(1 - 100)$ KeV.

In each of the two arrays $P_{sc}(B'_{st}(i), \mu_{ns}, (\omega_{st}(k), k = 1, k_{max}))$ and $P_{sc}(B'_{st}(i+1), \mu_{ns}, (\omega_{st}(k), k = 1, k_{max}))$ we then linearly interpolate on ω to derive $P_{sc}(B'_{st}(i), \mu_{ns}, \omega_l)$ and $P_{sc}(B'_{st}(i+1), \mu_{ns}, \omega_f)$ respectively. Finally, a linear interpola-

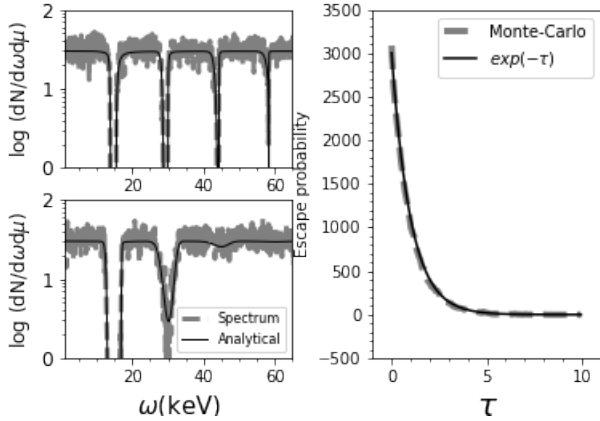


Figure 2. The simulation is performed for 1-0 Slab ($r_c = 1$ Km, $h_c = 100$ cm) for a uniform magnetic field $B' = 0.03$, $T_e = 5$ KeV, $\tau_T(\mu_i = 1) = 10^{-3}$. Left panel: Comparison of the Monte-Carlo and analytical estimates of the pencil beam spectra. The dashed line shows the Monte Carlo results and the solid line the analytical expectation. The top left panel is for $\mu_i = 0.1$ and the bottom left panel is for $\mu_i = 0.5$. Right panel: The distribution of the optical depth τ corresponding to the free paths generated for different scatterings. The dashed line shows the distribution generated in the Monte-Carlo simulation. The solid line represents the probability function $\exp(-\tau)$ scaled to the total number of scatterings.

tion on B' is carried out between these two values to obtain our desired quantity $P_{sc}(B'_{com}, \mu_{com}, \omega_{com})$.

3.8 Tests of the Monte Carlo code

We performed several checks and tests of our Monte-Carlo code and two of them are presented here.

3.8.1 Escape probability

First, we performed a test to confirm that the escape probability is modelled properly in our code. The simulation was performed for a thin slab 1-0 ($r_c = 1$ Km, $h_c = 100$ cm) for a uniform magnetic field $B' = 0.03$, $T_e = 5$ KeV, $\tau_T(\mu_i = 1) = 10^{-3}$. The escape probability of a photon traversing an optical depth $\delta\tau(\omega_i, \mu_i)$ is given by $\exp(-\delta\tau(\omega_i, \mu_i))$. We perform our simulations in real space so this corresponds to,

$$\delta\tau(\omega_i, \mu_i) = \frac{\delta\lambda}{\lambda} = n_e \langle \sigma_{sc}(\omega_i, \mu_i) \rangle_{f_e(p)} \delta\lambda$$

we generate the free paths $\delta\lambda$ in our simulation and store the corresponding $\delta\tau(\omega_i, \mu_i)$ values, the distribution of which is plotted in right panel of Fig-2. The thick gray dashed line is for the actual distribution of $\delta\tau$ produced by the Monte-Carlo simulations and the solid line represents the evaluation of the function $\exp(-\delta\tau(\omega_i, \mu_i))$. The two results match well, indicating that the escape probability is modelled accurately in our code.

3.8.2 Pencil beam injection test

Next, we performed a pencil beam injection test to confirm that the intensity removed from the pencil beam is in accordance with the analytical expectation from radiative transfer. The input parameters for this case is same as set in Sec.3.8.1. We injected a beam of

photons in a very small angle bin $\mu_i \pm \delta\mu_i$ with the energy in full continuum range (1-100 KeV). The escaping photons were collected in the same angle range $\mu_i \pm \delta\mu_i$. During the propagation many photons are scattered out of the beam. The output spectrum of the photons remaining in the pencil beam is expected to be given by just the optical depth profile as

$$I(\omega_i, \mu_i) = I_0 \exp(-\tau(\omega_i, \mu_i)) \quad (15)$$

where I_0 is the intensity of the injected continuum. The optical depth τ in the direction μ_i is given by

$$\tau(\omega_i, \mu_i) = n_e \langle \sigma_{sc}(\omega_i, \mu_i) \rangle_{f_e(p)} \frac{h}{\mu_i} \quad (16)$$

where h is vertical height of the slab, $\mu_i = \cos\theta_i$, θ_i is the angle between perpendicular to the slab and viewing direction and other symbols have their usual meaning.

The left panels of Fig-2 show the comparison between the expectation from Eq-15 with that of a Monte Carlo run for constant magnetic field $B' = 0.03$, $\tau_T = 10^{-3}$ and electron temperature $T_e = 5$ KeV. The top left panel is for $\mu_i = 0.1$ and the bottom left panel is for $\mu_i = 0.5$. The solid black lines represent the analytic estimate of the photon counts corresponding to the specific Intensity $I(\omega_i, \mu_i)$ derived from Eq-15 and the gray dashed lines represent the spectra from Monte-Carlo Simulations. They both agree well with each other. This test confirms that photon removal from the beam due to scattering is accurately modelled in our code.

4 RESULTS

In this section we present the phase averaged spectra in four angle bins. We will use the following abbreviated notation repeatedly for these 4 angle bins: μ_1 for the angle bin $0.0 < \mu_i \leq 0.25$, μ_2 for $0.25 < \mu_i \leq 0.5$, μ_3 for a $0.5 < \mu_i \leq 0.75$, and μ_4 for angle bin $0.75 < \mu_i \leq 1.00$.

Redshift: All the spectra are gravitational redshift corrected. The gravitational redshift factor near the neutron star surface is given by $\zeta = \sqrt{1 - 2GM_*/r}$, with mass of the neutron star $M_* = 1.4M_\odot$, $r \approx R_* = 10$ Km, gives the value $\zeta \approx 0.77$.

Continuum Model: The continuum model which we have used in all the spectra is HCUT (Eq- 8), for parameters $\Gamma = 0.91$, $\omega_{cut} = 25.5$ KeV and $\omega_{fold} = 9.0$ KeV.

Light bending: The photons are re-distributed in angle due to strong light bending effects near the stellar surface. We included this in computing the final observed spectra, as has also been done in Nishimura (2019). While computing the light bending two frames are considered: 1) a column centric frame $Gb(X^G, Y^G, Z^G)$ (as defined in Sec.3.7, 2) a star centric co-ordinate system $St(X^S, Y^S, Z^S)$ which has its origin at the center of the star and z axis along the spin axis of the neutron star. We will mention the ‘‘spectra without light bending’’ and ‘‘spectra with light bending’’ frequently. The spectra without light bending are produced in Gb frame and light bending effects are not incorporated, in this case μ is measured w.r.t the Z^G axis of the Gb frame. The spectra with light bending are produced in the St frame, computed after the inclusion of light bending. In this case μ is measured from the Z^S axis of the St frame. The angle between the spin axis of the neutron star and its magnetic axis is

denoted by θ_B . (see Appendix B for our implementation of light bending). To include the effect from both poles of the NS, we have assumed that the magnetic axis of the second pole is at an angle $(\pi + \theta_B)$ (diametrically opposite location) with the spin axis of the NS. To compute the phase average spectrum we have taken the average of the spectra produced by the two poles.

4.1 Monte Carlo simulations for Slab 1-0 with uniform magnetic fields

The emission geometry for this case is taken to be slab 1 – 0 (illuminated from below, $r_c = 1$ Km, $h_c = 100$ cm) for uniform field $B' = 0.03$, optical depth $\tau_r(\mu = 1) = 10^{-3}$. Photons are injected uniformly and isotropically at the base of the slab. It is assumed that if a photon hits the base of the slab then it is absorbed by the base.

The phase averaged redshifted spectra for flat continuum are shown in the left panel of the Fig-3. These clearly display the strong angle and energy dependence of the emergent intensity. At small angles $\mu \sim 1$ the cyclotron features are shallow and broad and at angles near 90° ($\mu \rightarrow 0$) they are deeper and sharper. The first harmonic (fundamental) has a complex shape in comparison to the second or higher harmonics. The fundamental is shallower than the second harmonic and displays emission wings contributed mainly by transition photons. In the low angle bins μ_3 and μ_4 , the emissions wings are more prominent. This results from the transition photons being heavily scattered in high angle bins due to large optical depth, and being thus redistributed to lower angle bins before escape. The filling in of the fundamental due to energy redistribution in multiple scatterings is therefore further exacerbated by added transition photons at the low angle bins. Observations also support that the fundamental is of a complex shape. In the source 4U0115+63 Heindl et al. (2004) found that the fundamental is modeled poorly by a Gaussian because of its very complex shape. Our results for a flat continuum are similar to those of SC17 for the slab geometry.

4.1.1 Effect of continuum

The right panel of the Fig-3 shows the phase averaged redshifted spectra for a highcut continuum model. We can see that the continuum significantly modifies the cyclotron lines features. For the highcut continuum, the prominent emission wings disappear, as the number of photons at higher energies which create transition photons at the fundamental are now much less. We find that the depth of the fundamental feature at low angles (μ_4) has increased. So, with the highcut continuum, the fundamental is found to be deeper than the first harmonic. These features are shared by the spectra reported in Schon07 although their plasma parameters and the continuum model are slightly different.

4.1.2 Effect of temperature

Fig-4 shows the effect of electron temperature on the cyclotron spectra. We have produced spectra for two different electron temperatures, 5 KeV and 10 KeV. For $T_e=10$ KeV, the cyclotron lines are found to be broader and shallower. At high angle bins μ_1, μ_2 , the broadening is also found to be asymmetric and skewed towards lower energies. This results from the asymmetry in the peaks of the line profiles $P_{sc}(\omega_i, \mu_i)$ due to the relativistic cut-off in energy (ω_n^{cut}) in higher angles bins.

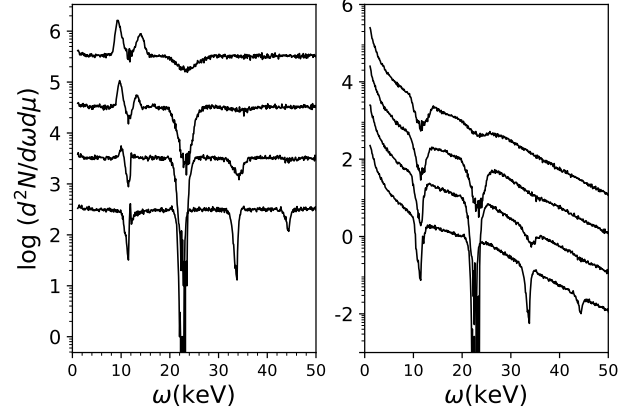


Figure 3. The phase averaged redshifted spectra, without light bending, for slab 1-0 geometry with uniform field $B' = 0.03$, uniform electron temperature $T_e = 5$ KeV and optical depth $\tau_T = 10^{-3}$. The left panel shows the spectra for flat continuum $f_p(\omega) = 1$ and the right panel shows the spectra for HCUT continuum with $\Gamma = 0.91$, $E_{cut} = 25.5$ KeV, $E_{fold} = 9.0$ KeV. The spectra are plotted for four different viewing bins $\mu_1, \mu_2, \mu_3, \mu_4$ from bottom to top.

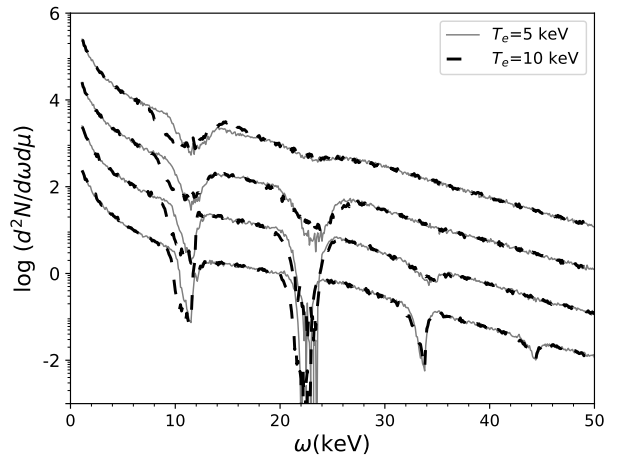


Figure 4. The phase averaged redshifted spectra, without light bending, for HCUT continuum and for the same parameters as in Fig-3 except for two different temperatures $T_e = 5$ KeV (solid gray lines) and $T_e = 10$ KeV (dashed black line.)

4.1.3 Effect of light bending

The left panel of Fig-5 shows the CRSF without (solid gray lines) and with light bending (black dashed lines) assuming the angle between the spin axis and magnetic axis, $\theta_B = 10^\circ$. The right panel in this figure contains two plots with light bending, one for $\theta_B = 10^\circ$ (gray solid line), and the other for $\theta_B = 45^\circ$ (black dashed lines). Note that μ in the case of spectra without light bending and that for the case with light bending are measured from two different axis, as already mentioned in the beginning of the Sec.4. The spectra with light bending represent the spin-phase averaged spectra which is normally observed from cyclotron line sources. Spectrum for any value of μ measured from the spin axis clearly includes the contribution from a range of μ values with respect to the magnetic

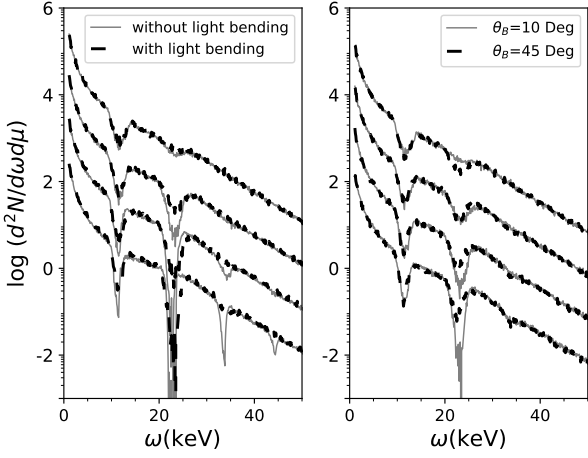


Figure 5. Left panel: comparison of spin phase averaged redshifted spectra with (dashed black) and without light bending (solid gray), for $\theta_B = 10^\circ$. Right panel: Spin phase averaged redshifted spectra with light bending for two different angles $\theta_B = 10^\circ$ (solid gray), and 45° (dashed black), between spin axis and magnetic axis. The input parameters are the same as in Fig-3. The spectra are plotted for four different viewing bins $\mu_1, \mu_2, \mu_3, \mu_4$ from bottom to top.

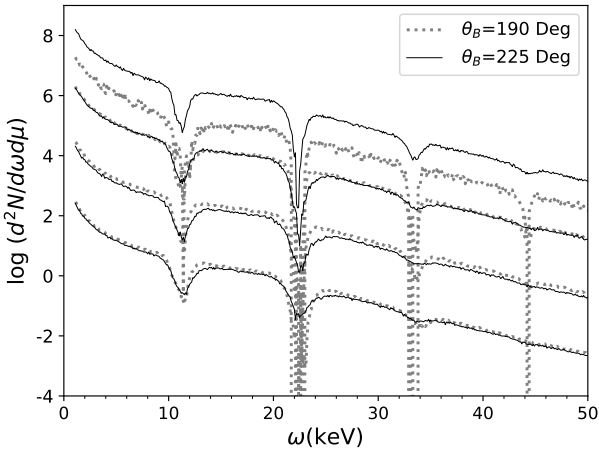


Figure 6. Phase averaged redshifted spectra with light bending for magnetic inclination $\theta_B = 190^\circ$ (broken gray), and $\theta_B = 225^\circ$ (solid black). The input parameters are the same as in Fig-3.

axis. Thus the spectra with light bending involve an average over those without light bending as can be seen in the left panel of Fig-5. This tends to wash out sharp, highly angle-dependent features in the spectrum as is evident from the figure - sharp, deep features become shallow and wide, and some features, for example, harmonics above the second, disappear altogether. The spectra at different angles look even more similar if the inclination angle between the spin axis and the magnetic axis is increased, as seen in the right panel of Fig-5 where an inclination angle of $\theta_B = 45^\circ$ is assumed. In Fig-6 we have shown the phase averaged spectra from a slab for angles $\theta_B = 190^\circ$ and $\theta_B = 225^\circ$ with the spin axis. Fig-7 shows the spin phase averaged redshifted spectra with light bending including both the poles of the NS, for $\theta_B = 10^\circ$ and $\theta_B = 45^\circ$.

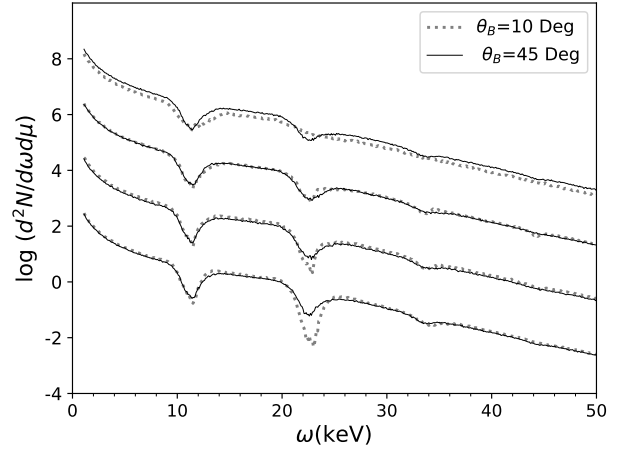


Figure 7. Phase averaged redshifted spectra with light bending including both poles of the NS, for magnetic inclination $\theta_B = 10^\circ$ (broken gray), and $\theta_B = 45^\circ$ (solid black). The input parameters are the same as in Fig-3.

The main consequence of light bending is that if the spectrum originates close to the neutron star surface where light bending is strong, the difference between spectra observed at different angles tends to diminish considerably (Fig-7). This also drastically reduces the spin phase dependence of the spectrum, as also pointed out by MB12. This suggests that strongly phase-dependent spectra should either originate at large heights from the stellar surface or have contributions from physically different regions, such as asymmetric opposite poles (MB12).

Observationally, both significant (e.g. GX 301-2 Heindl et al. (2004)) and small (e.g. V0332+53 Pottschmidt et al. (2005)) dependence of the CRSF on spin phase have been observed. The reason for such diversity is yet to be clearly understood, but is likely to lie in the diversity of emission geometry.

4.2 Accretion mound with accretion induced distorted magnetic fields

Cyclotron lines bear the signature of the distortion of the magnetic fields. In an accretion mound the magnetic field is severely distorted which could be reflected in the observed CRSFs.

The variation of B_r , B_z and $B = \sqrt{B_r^2 + B_z^2}$, along the radial direction r (in cylindrical co-ordinate system) in the optically thin top layer of a mound, are shown in Fig-8, for two different heights, 45 m, and 55m. The variation in B_r is higher than that in B_z along the radial direction r . It can be seen that the maximum variation occurs at $r \sim 700 - 800$ meter, and the maximum total field can reach a value of 2 - 6 times of the minimum.

The different panels (bottom and top) in Fig-9 show the redshifted spectra without light bending for mounds of height 45m and 55m, for different angle bins measured from the magnetic axis. We find that at lower angles, the cyclotron lines have a small depth and at higher angular bins, the depth is much larger. The width of the lines is found to be larger at all angles, compared to the width found for a constant magnetic field (Fig-3). The redshifted spectra from 45m mound (bottom of Fig-9), and at higher angular bins (μ_1 and μ_2) have cyclotron absorption features nearly at 7.7, 15.4, 30.8, 46.2 KeV. The pattern is primarily composed of two sets of line feature. One, ($\zeta\omega_n^{cyc}(B' \approx 0.02)$) from the region of the lower

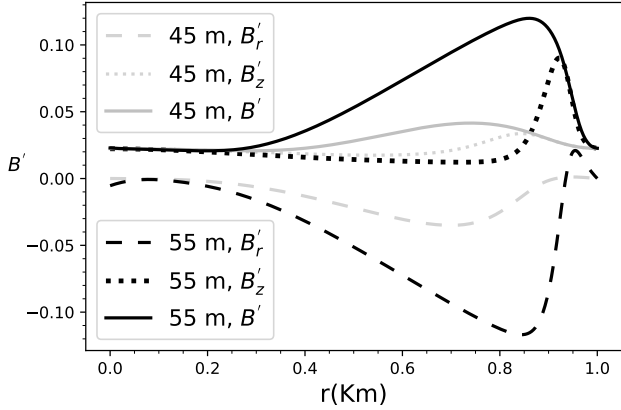


Figure 8. Radial dependence of the magnetic field components at the top of the two mounds, of height 45m and 55m respectively.

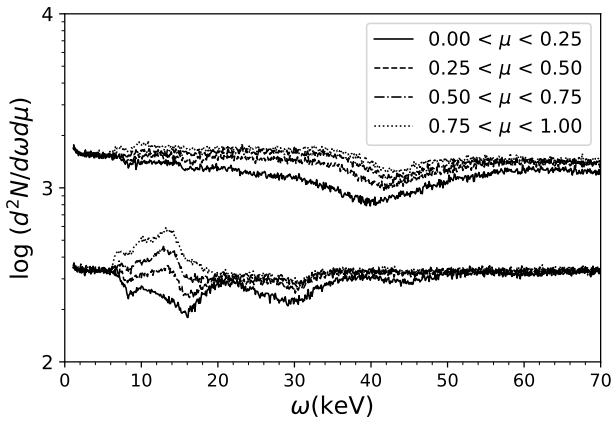


Figure 9. Spin phase averaged redshifted spectra without light bending for flat continuum from two mounds of height 45m (bottom) and 55m (top). The spectra are produced for a geometry of slab 1-0 with uniform electron temperature $T_e = 5$ KeV and $\tau_T = 10^{-3}$, for four different μ bins. The density profile is derived from the Paczynski equation of state (Paczynski 1983).

magnetic field $B' \approx 0.02$, contributing at 7.7, 15.4, 23.1, 30.8, 38.5, ... KeV, and the second line pattern ($\zeta \omega_n^{cyc}(B' \approx 0.04)$) from near the maximum of the magnetic field $B' \approx 0.04$, contributing at 15.4, 30.8, 46.2.. KeV. These two patterns overlap and create prominent absorption features at 7.7, 15.4, 30.8, 46.2 KeV. Features at 23.1, 38.5 KeV, contributed only by the region where $B' = 0.02$ and they are not deep enough to be visible in the composite spectrum.

Spectra from mounds with 55m height (Fig-9) share the same qualitative features as those discussed for the 45m mound. The magnetic distortion is larger in this case, and the line energies are spread correspondingly further. The effective widths of the line features are also significantly larger, particularly for features originating in the high field regions. For the 55m mound the entire spectrum is dominated by a single wide feature near 40 KeV (redshifted) corresponding to the fundamental originating near the field maximum of $B' \approx 0.12$.

Clearly, the CRSF line energies produced from the accretion mounds do not follow the classical harmonic ratio for line features,

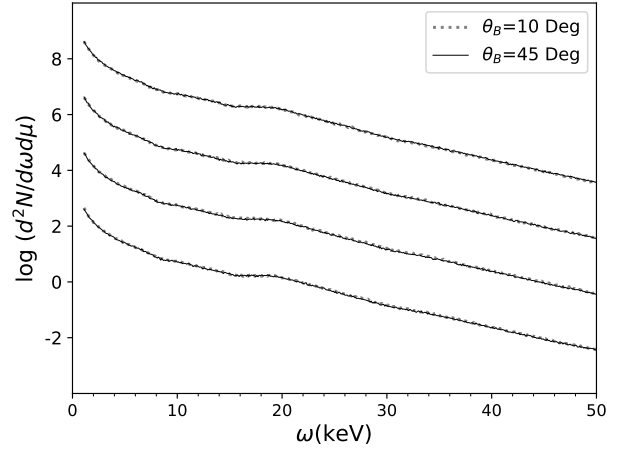


Figure 10. Spin phase averaged redshifted spectra from 45m mound for highcut continuum including the light bending for two angles $\theta_B = 10^\circ, 45^\circ$ between the spin axis and magnetic axis. The spectra are plotted for four different viewing bins $\mu_1, \mu_2, \mu_3, \mu_4$ from bottom to top. The input parameters are the same as in Fig-9.

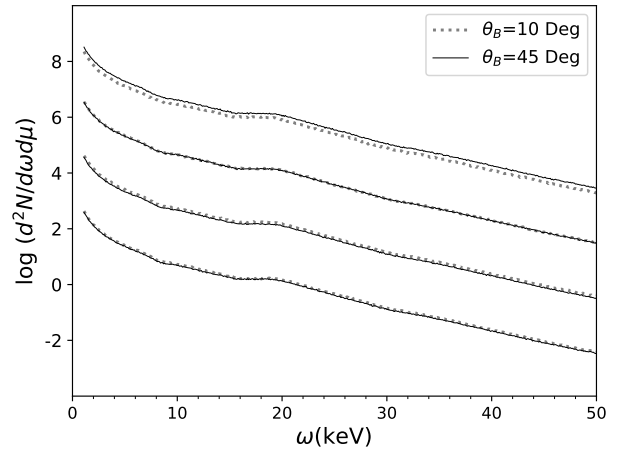


Figure 11. Same as Fig-10 but including both the poles of the NS.

as they are composed of lines due to different field strengths in different regions. Examples of anharmonic spacing of cyclotron features exist also in observed sources. For example the phase averaged spectra of 4U0115+63 contain cyclotron features at 16.4, 23.2, 31.9, 48 KeV (Coburn et al. 2002). However such anharmonicity is not easy to detect in all cases due to the uncertainties in line energy estimation arising from our lack of knowledge of the true underlying continuum.

Line features in observed sources are typically quite broad, for example the width of the fundamental is ~ 6.4 KeV for Her X-1, ~ 9 KeV for 4U0352+309, ~ 8 KeV for GX 301-2, ~ 7 KeV for Cen X-3 etc (Coburn et al. 2002). In Fig-9 the widths of the first three harmonics are found to be nearly 3, 6, 7 KeV. So, the widths of features obtained in our mound spectra are comparable to the observed values.

In Fig-10, we present the spin phase averaged redshifted spectra incorporating light bending for two angles $\theta_B = 10^\circ$ and 45° ,

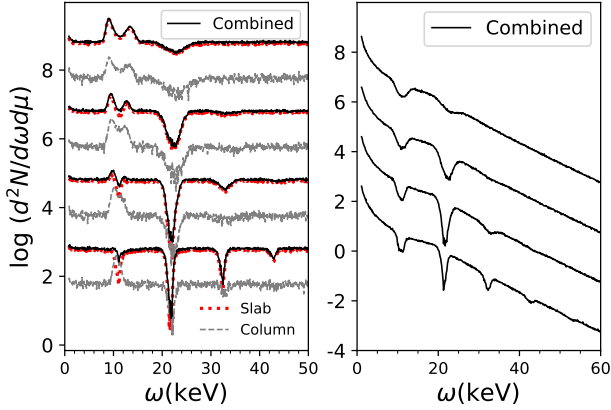


Figure 12. Left panel: Spin phase averaged redshifted spectra without light bending from accretion column for flat continuum in four different angle bins ($0.0 < \mu_1 \leq 0.25$, $0.25 < \mu_2 \leq 0.5$, $0.5 < \mu_3 \leq 0.75$, $0.75 < \mu_4 \leq 1.0$). Red dotted lines: spectra from top slab (*SI*), Gray dashed lines: spectra from the sides (*Cy*), Black solid lines: total spectra of *SI* and *Cy*. Right panel: Spin phase averaged redshifted spectra from accretion column for highcut continuum in four different angle bins. The spectra are the sum of those from *SI* and *Cy*.

between the spin axis and magnetic axis, and for two angle bins μ_1 and μ_4 , with respect to the spin axis. The angular averaging involved in this causes the spectra for different angle bins to look very similar. Relatively shallow spectral features near 7, 15 and 30 KeV are recognizable in these spectra, as also in the spectra including both poles of the NS (Fig-11).

4.3 Accretion column

In this section we present the spectra produced by the accretion column for high luminosity sources. We take the plasma density profile of Becker & Wolff (2007). We assume that the mass accretion-rate is $\sim 10^{-8} M_{\odot}/\text{year}$, which gives a density of about $2 \times 10^{25} \text{ cm}^{-3}$ near the base (computed $\sim 1 \text{ cm}$ above the base) and $\sim 2.7 \times 10^{20} \text{ cm}^{-3}$ at the top of the column. We simulate an optically thin layer with perpendicular Thompson optical depth τ_T of 10^{-3} . Such a layer has a thickness of about 10^{-5} cm at the base and $\sim 5 \text{ cm}$ at the top. For simplicity, we model the inner boundary of the simulation volume as a truncated cone (Fig-1). The dimensions of inner conical surface using the density profile of Becker & Wolff (2007) is computed in appendix A. Given the non-linear dependence of density on z , τ_T (Eq-A1) to this conical surface somewhat exceeds 10^{-3} except at the two ends. The photons are injected at surface of this cone. The simulation region which is bounded by the surface of the column and surface of the cone can be assumed to consist of

- 1) A thin slab at the top (*SI*): It is situated at the top of the circular surface of the truncated cone, having height ($\sim 5 \text{ cm}$) corresponding to $\tau_T = 10^{-3}$. The magnetic field intensity inside *SI* is assumed to be uniform ($B' \approx 0.022$).
- 2) A near-cylindrical shell *Cy*: The region between the accretion column and the side walls of the truncated cone (Fig 1), having height $z_b = z_c - z_t$. Due to the large height of *Cy*, the variation of the magnetic field is noticeable, $B' \approx 0.03$ at the bottom and $B' \approx 0.022$ at the top.

The left panel of the Fig-12 shows the redshifted spectra for

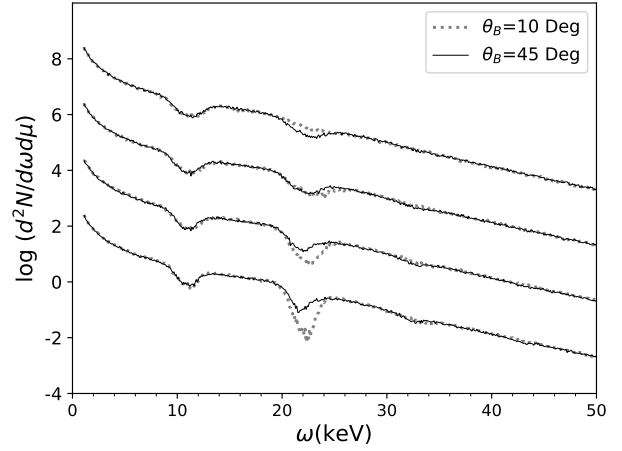


Figure 13. Spin phase averaged redshifted spectra from accretion column including light bending for HCUT continuum for two angles $\theta_B = 0^\circ, 45^\circ$ between the spin axis and magnetic axis. The spectra are the sum of those from *SI* and *Cy*, for four different angle bins ($0.0 < \mu_1 \leq 0.25$, $0.25 < \mu_2 \leq 0.5$, $0.5 < \mu_3 \leq 0.75$, $0.75 < \mu_4 \leq 1.0$).

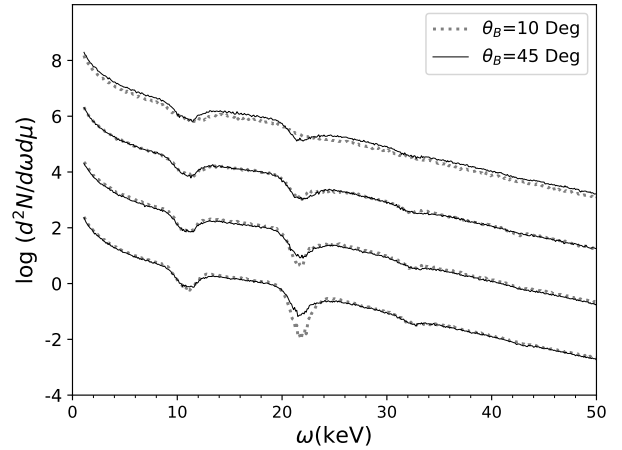


Figure 14. Same as Fig-13, including the contribution from both poles of the NS.

flat continuum. In this figure, the red dotted line corresponds to the output spectrum resulting from *SI*, the gray dashed line corresponds to the output spectrum obtained from *Cy*, and the black solid curve represents the combined spectrum generated from *SI* and *Cy*. The spectra produced in *SI* are found to be qualitatively similar to those we found from a 1-0 slab with a constant field. We find various harmonically spaced dips which are sharper at high angle bins and shallower at low angle bins. At low angle bins, a prominent presence of emission wings has also been found. The variation in the field strength within *Cy* broadens the line profile, and the line centres represent the average of the field intensity. In this case, we see two prominent features, an emission wing at 10 keV, and an absorption feature at 17 KeV.

The combined spectrum, obtained by summing the *SI* and the *Cy* spectra, have line features shallower than those for *SI*, and the fundamental appears in emission at all angle bins. Spectra generated

with highcut continuum are shown in the right panel of the Fig–12. Due to the reduction in the number of transition photons, in this case the emission features are suppressed. The spectra are found to depend significantly on the angle from the magnetic axis. In the lowest angle bin μ_4 the fundamental is deeper than the second harmonic, while at other angle bins it is the opposite. At the highest angle bin μ_1 up to five absorption features can be discerned.

Fig–13 shows the spin phase averaged redshifted spectra for two values of θ_B , 10° and 45° , including the light-bending effects. For $\theta_B = 10^\circ$, we find a variation of cyclotron line features with μ , as the effect of light bending at the top of Cy is significantly smaller than at the bottom (near NS surface). For $\theta_B = 45^\circ$, we find the spectra to be quite similar in all angle bins due to a greater angular averaging of the spectra. We can see the same effect in the phase averaged combined spectra from both poles of the NS (Fig–14).

5 CONCLUSIONS

The main conclusions of our computations are summarized below.

- In the literature it is customary to compute the locally emergent spectra as a function of the angle from the magnetic axis. We find that the spin phase averaged spectra including general relativistic effects, representing what would be seen by a distant observer, differ substantially from the above. It is therefore essential to compute the latter when a comparison with observed spectra have to be made.
- The extent of angular averaging involved in the formation of observed spectra depends on the amount of light bending, which is very severe near the stellar surface, and reduces with altitude. If the emission region is located very close to the stellar surface then the observed spectra are rendered nearly independent of viewing angle unless the local emergent spectra are very strongly anisotropic, as in the case of a uniform field slab. If the emission region extends farther away from the star, then the dependence on viewing angle becomes more perceptible.
- The profiles of the cyclotron features, in particular of the fundamental, are strongly dependent on the shape of the input continuum. The harder the continuum, the more is the population of transition photons which tend to fill in the fundamental feature and create emission wings. This is seen very clearly in the spectra produced by a flat continuum. On the other hand, for a power-law continuum with exponential cutoff the effect of transition photons is minimal and the emission wings are virtually absent.
- For a thin slab with uniform field, the local emergent spectra are strongly dependent on the angle from the magnetic axis. Deep and narrow features are seen at angles normal to the magnetic field, and the features are found to be broader and shallower close to the magnetic axis. For a distant observer, the wider features are found to dominate the spectra and harmonics above the second are washed out. The line widths (~ 2 KeV) are found to be relatively small compared to those usually seen in most X-ray pulsars.
- Spectra from accretion mounds show very broad and shallow lines with overlapping features from subsequent harmonics. For a distant observer, up to three distinct features are visible. These features are not necessarily harmonically spaced, and their widths reach up to ~ 10 KeV, not unlike some observed features but wider than the average seen in most sources.
- The accretion column with dipole field produces spectral features of intermediate width. They are asymmetric and somewhat anharmonically spaced. The spectra viewed by a distant observer show detectable anisotropy, but features higher than the second harmonic are washed out.

The emission geometries we have explored in this work do generate features similar to those observed in some sources. But our simulations do not appear to reproduce the full range of observed behavior in cyclotron spectra. In particular, more than three prominent harmonic features have been observed in a few sources, like 4U0115+63, and in our simulation the higher harmonics are found to nearly disappear after applying the highcut continuum. This indicates a larger diversity in the characteristics of the emission regions in different sources. The existence of many prominent harmonic features and strong spin phase dependence may suggest emission regions relatively far from the stellar surface, and perhaps require more complex geometry than those explored in this work. The Monte-Carlo code developed by us has the ability to simulate many such complex situations, which will be attempted in the future.

ACKNOWLEDGEMENTS

The research work is funded by the the Council of Scientific and Industrial Research (CSIR), University Grants Commission (UGC) and Govt. of India. The authors want to thank the Inter University Centre for Astronomy and Astrophysics (IUCAA) for the research facilities. We sincerely acknowledge the use of high performance computing facilities at IUCAA, and in C-DAC, Pune. We want to thank the anonymous referee for the valuable comments and suggestions which substantially improved the contents of the paper.

DATA AVAILABILITY

The data underlying this article will be shared on reasonable request to the corresponding author.

REFERENCES

- Alexander S. G., Meszaros P., 1991, *ApJ*, **372**, 565
Alexander S. G., Meszaros P., Bussard R. W., 1989, *ApJ*, **342**, 928
Araya R. A., Harding A. K., 1996, *A&AS*, **120**, 183
Araya R. A., Harding A. K., 1999, *ApJ*, **517**, 334
Becker P. A., Wolff M. T., 2007, *ApJ*, **654**, 435
Becker P. A., et al., 2012, *A&A*, **544**, A123
Beloborodov A. M., 2002, *ApJ*, **566**, L85
Bonazzola S., Heyvaerts J., Puget J. L., 1979, *A&A*, **78**, 53
Bulik T., Meszaros P., Woo J. W., Hagase F., Makishima K., 1992, *ApJ*, **395**, 564
Bulik T., Riffert H., Meszaros P., Makishima K., Mihara T., Thomas B., 1995, *ApJ*, **444**, 405
Coburn W., Heindl W. A., Rothschild R. E., Gruber D. E., Kreykenbohm I., Wilms J., Kretschmar P., Staubert R., 2002, *ApJ*, **580**, 394
Freeman P. E., Lamb D. Q., Wang J. C. L., Wasserman I., Loredò T. J., Fenimore E. E., Murakami T., Yoshida A., 1999, *ApJ*, **524**, 772
Gil J. A., Melikidze G. I., Mitra D., 2002, *A&A*, **388**, 235
Harding A. K., Daugherty J. K., 1991, *ApJ*, **374**, 687
Harding A. K., Preece R., 1987, *ApJ*, **319**, 939
Harding A. K., Meszaros P., Kirk J. G., Galloway D. J., 1984, *ApJ*, **278**, 369
Heindl W. A., Rothschild R. E., Coburn W., Staubert R., Wilms J., Kreykenbohm I., Kretschmar P., 2004, in Kaaret P., Lamb F. K., Swank J. H., eds, American Institute of Physics Conference Series Vol. 714, X-ray Timing 2003: Rossi and Beyond. pp 323–330 ([arXiv:astro-ph/0403197](https://arxiv.org/abs/astro-ph/0403197)), doi:10.1063/1.1781049
Isenberg M., Lamb D. Q., Wang J. C. L., 1998a, *ApJ*, **493**, 154
Isenberg M., Lamb D. Q., Wang J. C. L., 1998b, *ApJ*, **505**, 688
Latal H. G., 1986, *ApJ*, **309**, 372
Meszaros P., Nagel W., 1985, *ApJ*, **299**, 138

- Meszáros P., Nagel W., Ventura J., 1980, *ApJ*, **238**, 1066
 Meszáros P., Harding A. K., Kirk J. G., Galloway D. J., 1983, *ApJ*, **266**, L33
 Mukherjee D., Bhattacharya D., 2012, *MNRAS*, **420**, 720
 Nagel W., 1980, *ApJ*, **236**, 904
 Nagel W., 1981a, *ApJ*, **251**, 278
 Nagel W., 1981b, *ApJ*, **251**, 288
 Nishimura O., 2003, *PASJ*, **55**, 849
 Nishimura O., 2005, *PASJ*, **57**, 769
 Nishimura O., 2008, *ApJ*, **672**, 1127
 Nishimura O., 2011, *ApJ*, **730**, 106
 Nishimura O., 2019, *PASJ*, **71**, 42
 Paczynski B., 1983, *ApJ*, **267**, 315
 Payne D. J. B., Melatos A., 2004, *MNRAS*, **351**, 569
 Pottschmidt K., et al., 2005, *ApJ*, **634**, L97
 Poutanen J., Gierliński M., 2003, *MNRAS*, **343**, 1301
 Pravdo S. H., Bussard R. W., 1981, *ApJ*, **246**, L115
 Schönherr G., Wilms J., Kretschmar P., Kreykenbohm I., Santangelo A., Rothschild R. E., Coburn W., Staubert R., 2007, *A&A*, **472**, 353
 Schwarm F. W., et al., 2017a, *A&A*, **597**, A3
 Schwarm F. W., et al., 2017b, *A&A*, **601**, A99
 Shabad A. E., 1975, *Annals of Physics*, **90**, 166
 Sina R., 1996, PhD thesis, University of Maryland
 Sokolov A. A., Ternov I. M., 1968, Synchrotron radiation. Akademie-Verlag, Berlin
 Staubert R., et al., 2019, *A&A*, **622**, A61
 Truemper J., Sacco B., Pietsch W., Reppin C., Kendziorra E., Staubert R., 1977, *Mitteilungen der Astronomischen Gesellschaft Hamburg*, **42**, 120
 Wang J. C. L., Wasserman I. M., Salpeter E. E., 1988, *ApJS*, **68**, 735
 Yahel R. Z., 1979, *ApJ*, **229**, L73

This paper has been typeset from a \LaTeX file prepared by the author.

APPENDIX A: ESTIMATES OF DIMENSION OF THE CONICAL SOURCE SURFACE

Here we have estimated the dimensions of the conical injection surface and the volume in which radiative transfer take place in an accretion column (Case-III, Fig-1). We get a Thompson optical depth $\tau_T(l)$ by integrating on density $n_e(z)$ (Eq-5) over depth l . Where, l is measured from the top of the column. In terms of altitude z from the base, $l = z_c - z$, where z_c is the total height of the column (Fig 1). We compute the Thompson optical depth as a function of altitude $\tau_T(z)$. An inversion is then performed to get the height z_T as a function of Thompson optical depth τ_T .

$$z_T(\tau_T) = \frac{z_c}{\ln(a)} \ln \left(1 + (a-1) \exp \left(-\frac{\tau_T \ln(a)}{n_0 \sigma_T z_c} \right) \right) \quad (\text{A1})$$

where $a = 7/3$, z is measured from the bottom of the column and n_0 is a parameter having the dimension of number density:

$$n_0 = \frac{\dot{M}_c}{\pi r_c^2 v_{ff} m_{He}} \quad (\text{A2})$$

The height of the truncated cone can be computed for Thompson optical depth $\tau_T = 10^{-3}$ using Eq-A1

$$z_b = z_T(\tau_T = 10^{-3}) \quad (\text{A3})$$

Next, we have estimated the radius of the upper and lower circular base (r_t, r_b), with horizontal Thompson optical depth $\tau_t = 10^{-3}$ of the cone (Fig-1). While computing (r_t, r_b) we assume that the density n_e does not vary along the horizontal direction. The thickness of the optically thin layer r_{tt} at the height z_b and, r_{bb} at the bottom of the column can be computed as

$$r_{tt} = \frac{\tau_T (= 10^{-3})}{n_e(z_b) \sigma_T}, \quad r_{bb} = \frac{\tau_T (= 10^{-3})}{n_e(z_c) \sigma_T} \quad (\text{A4})$$

where z_c is a very small height above the base. Note that the $n_e(z) \rightarrow \infty$ as $z \rightarrow 0$ so to we have taken $z_c = 1$ cm, where the value of r_{bb} is of order 10^{-3} cm. The radius of the top and bottom circular base of the cone can be computed as (Fig-1),

$$r_t = r_c - r_{tt}, \quad r_b = r_c - r_{bb} \quad (\text{A5})$$

The half angle of the apex of cone is then

$$\theta_h = \tan^{-1}((r_b - r_t)/z_b) \quad (\text{A6})$$

The next step is to inject photons isotropically on the surface of the cone. The PDF of isotropic photon injection is given by the fractional area. After using the inverse function method we can get equations for r and ϕ as,

$$r = \sqrt{\left(r_t^2 + \left(r_b^2 - r_t^2 \right) \xi \right)}, \quad \phi = 2\pi \xi \quad (\text{A7})$$

where ξ is a uniform variate. The altitude z corresponding to r can be obtained from the geometry of the cone,

$$z = (r_b - r)/\tan(\theta_h) \quad (\text{A8})$$

so the photon injection is performed at the position

$$x_{inj} = r \cos(\phi), \quad y_{inj} = r \sin(\phi), \quad z_{inj} = z \quad (\text{A9})$$

We select the propagation angle θ_{inj}, ϕ_{inj} for the photon. For the injection of a photon at $x_{inj}, y_{inj}, z_{inj}$ in a certain direction θ_{inj}, ϕ_{inj} we consider a tangent plane at the point $x_{inj}, y_{inj}, z_{inj}$. The photons are injected outwards of the tangent plane, and away from the surface of the cone. The injection angles are chosen first in a local co-ordinate system and then transformed to the global co-ordinate system. The global co-ordinate system has its origin at the center of the base of the column, and its z axis is aligned with the magnetic axis. The local co-ordinate system has its origin at $x_{inj}, y_{inj}, z_{inj}$ and its z axis is along the slant surface, pointing towards the apex. The x axis of the local co-ordinate system is chosen to be perpendicular to the tangent plane, and pointed towards the outward direction. Two rotations by angles θ_h, ϕ are needed to transform the propagation angles from the local frame to the global frame. In the local frame the angle θ''_{inj} is chosen in the range $(0, \pi)$, but ϕ''_{inj} is chosen to be within the range $(-\pi/2, \pi/2)$ to ensure the outward propagation of the photon. The direction cosines corresponding to $\theta''_{inj}, \phi''_{inj}$ in the local frame are,

$$\begin{aligned} \Omega''_x &= \sin \theta''_{inj} \cos \phi''_{inj} \\ \Omega''_y &= \sin \theta''_{inj} \sin \phi''_{inj} \\ \Omega''_z &= \cos \theta''_{inj} \end{aligned} \quad (\text{A10})$$

which may be transformed to the global frame via two rotations,

$$\begin{pmatrix} \Omega_x \\ \Omega_y \\ \Omega_z \end{pmatrix} = \begin{pmatrix} \cos(\theta_h) \cos(\phi) & -\sin(\phi) & -\sin(\theta_h) \cos(\phi) \\ \cos(\theta_h) \sin(\phi) & \cos(\phi) & -\sin(\theta_h) \sin(\phi) \\ \sin(\theta_h) & 0 & \cos(\theta_h) \end{pmatrix} \begin{pmatrix} \Omega''_x \\ \Omega''_y \\ \Omega''_z \end{pmatrix} \quad (\text{A11})$$

from which we compute the injection angles θ_{inj}, ϕ_{inj} :

$$\theta_{inj} = \tan^{-1} \left(\frac{\sqrt{\Omega_x^2 + \Omega_y^2}}{\Omega_z} \right)$$

$$\phi_{inj} = \tan^{-1} \left(\frac{\Omega_y}{\Omega_x} \right)$$

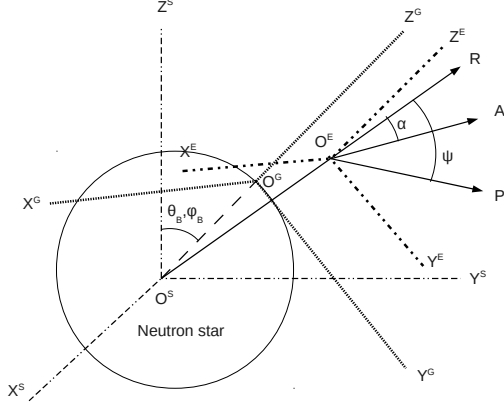


Figure A1. The figure shows schematic diagram used to compute the light bending. The St frame has the center at O^S , the Gb frame has the center at O^G and the Es frame has the center at O^E .

APPENDIX B: LIGHT BENDING

The photon trajectory near the compact object bends due the strong gravitational field. The photon which is emitted at the point R_x, R_y, R_z ($R\hat{R}$) (measured from center of compact object) at an angle α measured from the radial direction \hat{R} , reaches the observer at infinity at an angle ψ (measured from the radial direction \hat{R}). A very simple but approximate formula of gravitational light bending has been derived by Beloborodov (2002).

$$1 - \cos \alpha = (1 - \cos \psi) \left(1 - \frac{r_g}{R}\right) \quad (\text{B1})$$

where $r_g = 2GM/c^2$ is the Schwarzschild radius of the neutron star. The formula is valid up to $\alpha = 90^\circ$, and beyond that the error grows rapidly. If the unit vectors along the direction of emission (α measured from the radial direction) of a photon at the neutron star surface and the direction of escape of the photon to the observer (ψ measured from the radial direction) are $\mathbf{n}_\alpha, \mathbf{n}_\psi$ respectively, then from Poutanen & Gierliński (2003) we get,

$$\mathbf{n}_\psi = \frac{\sin \psi}{\sin \alpha} \mathbf{n}_\alpha - \frac{\sin(\psi - \alpha)}{\sin \alpha} \hat{R} \quad (\text{B2})$$

Fig-A1 shows the schematic diagram of light bending and the geometry.

- i) $St(X^S, Y^S, Z^S)$: The reference frame with origin O^S at the center of the star with its z axis along the spin axis of the neutron star.
- ii) $Gb(X^G, Y^G, Z^G)$: The reference frame with its origin at the center of the bottom circular surface O^G of the accretion column with its z axis parallel to the magnetic axes of the neutron star.
- iii) $Es(X^E, Y^E, Z^E)$: The reference frame with origin O^E at the point where photon escapes and all its axes parallel to those of the frame Gb .

We compute the light bending in a local frame Es (light bending angle is the same in the Gb frame since the axes of Es and Gb are parallel) and then the direction of light bending has been obtained in the frame St . To compute the light bending in frame Es we have represented the vectors in Eq-B2, in the local frame Es . Let $\mathbf{n}_\alpha = \mathbf{O}^E \mathbf{A} / |\mathbf{O}^E \mathbf{A}|$ be the direction at which the photon emerges, $\mathbf{n}_\psi = \mathbf{O}^E \mathbf{B} / |\mathbf{O}^E \mathbf{A}|$ be the direction in which photon reaches the observer after light bending, and $\hat{R} = \mathbf{O}^S \mathbf{R} / |\mathbf{O}^S \mathbf{A}|$ be the radial vector from the center of the neutron star to the emergence point.

The photons are injected in the frame Gb at angle θ_i, ϕ_i measured from the Z^G axis so

$$\begin{aligned} n_{\alpha x} &= \sin \theta_i \cos \phi_i \\ n_{\alpha y} &= \sin \theta_i \sin \phi_i \\ n_{\alpha z} &= \cos \theta_i \end{aligned} \quad (\text{B3})$$

\hat{R} can be written as

$$\hat{R} = \frac{\mathbf{R}_* + \mathbf{O}^G \mathbf{O}^E}{|\mathbf{R}_* + \mathbf{O}^G \mathbf{O}^E|} \quad (\text{B4})$$

\hat{R} can be represented in the frame Gb . The angle α can now be obtained with the dot product of $\hat{R}, \mathbf{n}_\alpha$

$$\alpha = \cos^{-1}(\hat{R} \cdot \mathbf{n}_\alpha) \quad (\text{B5})$$

using the values of $\mathbf{n}_\alpha, \hat{R}, \alpha$ and putting the value of ψ from Eq-B1 in terms of α in Eq-B2 one can get the value of the components of the unit vector of light bending \mathbf{n}_ψ in the Gb frame. This vector which is computed in the frame Gb can be transformed to the frame St by making two rotations in angle θ_B, ϕ_B . Here θ_B, ϕ_B are the polar and azimuth angle of magnetic field axis ($O^G Z^G$) in St frame.